International Journal of Nanomedicine

Dovepress
Taylor & Francis Group

Open Access Full Text Article

ORIGINAL RESEARCH

Multimodal Imaging By Polydopamine Nanoparticles for Effective Pre- and Intra-Operative Lymph-Node Screening in Gastric Cancer Using Mice Model

Yanrui Liang[1,*], Guodong Shen[1,*], Keyu He[1,*], Weisheng Wang[1,*], Bing Xiao[1,*], Tian Lin[1], Huilin Huang[1], Zhenyuan Li[1], Yingxin Ren[1], Zean Wang[1], Yiheng Luo[1], Weihong Guo[1], Yanfeng Hu[1], Guoxin Li[1,2]

[1]Department of General Surgery, Guangdong Provincial Key Laboratory of Precision Medicine for Gastrointestinal Tumor, Nanfang Hospital, Southern Medical University, Guangzhou, Guangdong, 510515, People's Republic of China; [2]Cancer Center of Beijing Tsinghua Changgung Hospital, School of Clinical Medicine, Tsinghua Medicine, Tsinghua University, Beijing, People's Republic of China

*These authors contributed equally to this work

Correspondence: Guoxin Li; Yanfeng Hu, Department of General Surgery, Guangdong Provincial Key Laboratory of Precision Medicine for Gastrointestinal Tumor, Nanfang Hospital, Southern Medical University, 1838 North Guangzhou Ave, Guangzhou, Guangdong, 510515, People's Republic of China, Tel +0086-20-6164-1681, Email gzliguoxin@163.com; yfenghu@qq.com

Introduction: Systematic lymphadenectomy is crucial in gastric cancer surgery for improving patient prognosis. However, current clinical lymph node (LN) mapping relies on fragmentary single-modal imaging agents, which suffer from low accuracy in N-staging and lack integration between preoperative and intraoperative visualization.

Methods: We developed polydopamine-based nanoparticles (PEG-PDA@IR820/Gd$(NH_2)_2$) termed PPIG NPs) as a unified multi-modal imaging agent for magnetic resonance (MR), optical, near-infrared (NIR) fluorescence, and thermal LN mapping. PPIG NPs were synthesized in three distinct size ranges (50–100 nm, 100–150 nm, 150–200 nm). Their imaging performance and lymphatic drainage kinetics were evaluated in vivo in a mouse model. Furthermore, the efficacy of PPIG NPs for LN identification was validated in fresh human gastric and colon cancer specimens via subserosal injection.

Results: The differently sized PPIG NPs exhibited tunable and size-dependent lymphatic drainage and retention. In mice, they enabled integrative pre-operative (MR) and intra-operative (optical/NIR fluorescence/thermal) multimodal mapping of popliteal LNs. In human specimens, PPIG NPs specifically delineated lymphatic vessels and LNs. Guided by this dual-modal (optical/NIR) mapping, lymphadenectomy in human gastric specimens achieved a significantly higher LN yield compared to conventional visual inspection (mean number: 55.4 vs 36.8, $p < 0.05$). The approach also facilitated the precise identification of residual lymphatic vessels post-dissection.

Conclusion: PPIG NPs provide an integrative pre- and intra-operative multimodal LN mapping platform. This strategy, enabling "see-before-cut" planning and "trace-while-cutting" navigation, demonstrates superior accuracy for LN and lymphatic vessel identification compared to current fragmentary techniques, showing promising potential for guiding precise lymphadenectomy in gastric cancer.

Keywords: gastric cancer, lymph node mapping, lymphatic vessels, polydopamine-based nanoparticles, systemic lymphadenectomy

Introduction

Gastric cancer (GC) have become a global public health threat. In 2020, there were 770,000 deaths because of GC globally.[1] In East Asia, locally advanced gastric cancer (AGC) is still the main challenge in the treatment of GC. As lymph-node (LN) metastasis is an essential factor associated with prognosis of AGC patients, complete resection with standardized LN dissection (*D2*) is important for AGC.[2] For GC has a complex lymphatic drainage system and multiple lymph-node stations, the precise LN imaging is a vital technique for surgeons to visualize LNs pre- and intra-operatively

https://doi.org/10.2147/IJN.S555760
Received: 20 August 2025
Accepted: 23 January 2026
Published: 4 February 2026

while performing LN dissection.[3] However, discrepancies between different LN mapping modes make consistency in pre- and intra operative LN mapping challenging.

Endoscopic ultrasound, computed tomography, and magnetic resonance imaging (MRI) can be used for pre-operative LN mapping.[4] Owing to its sensitivity for soft tissue lesions, MRI has been the most widely applied.[5,6] However, its relative low accuracy for N staging (N followed by a number from 0 to 3 indicates whether the cancer has spread to lymph nodes near stomach), ranging from 52.17% to 71%, hampers its clinical application in gastrointestinal tumor diagnosis.[7–10] Moreover, inconsistency between pre-operative LN mapping and intraoperative mapping is one of the most important factors influencing the surgical outcome.[11] This might due to the undetectable during surgery for current clinical MRI contrast $Gd(NH_2)_2$.

During surgery, visible dyes have been used, such as carbon particles and near-infrared (NIR) fluorescence imaging agents, including indocyanine green (ICG), to map LNs. Nano-carbon particles have been used to image invasive breast, colorectal, and other cancers.[12,13] Owing to their black color and proper size (≈ 100nm), carbon nanoparticles can precisely delineate the lymphatic system.[14–16] However, nano-carbon particles can only be used for optical imaging[17] and may not fully reveal LNs due to the abundance of peri-gastric fat. Pathological outcomes, including inflammation, fibrosis, and tumorigenesis, further limit their application in clinical diagnosis and therapy.[18] Recently, NIR fluorescent dyes such as ICG have received increasing attention for clinical applications as they offer several advantages, including optimal tissue penetration in biological samples, decreased light scattering, and the ability to stain both LNs and the lymphatic route.[19] Despite these advantages, the application of NIR fluorescent dyes in clinical practice remains limited. The lack of coloration ability hinders the simplicity of LN mapping. Moreover, some clinical studies have indicated that LN detection using ICG is associated with a high false-negative rate and the possibility of leakage into the surgical field.[20–23] This may be due to its small molecular size and consequent diffusion into the blood system. In addition to optical imaging and NIR fluorescent imaging, thermal imaging is valued for its non-invasive nature and ease of handling.[24–26] Thermal imaging is used to study lymph drainage in malignant melanoma and oral squamous cell carcinoma.[27,28] By using a NIR photothermal LN-specific material, it would be possible to "light up" the LNs in a NIR thermal image for GC LN mapping.

Multimodal LN mapping agents may outdo pre- and intra-operative LN mapping modalities to improve the current LN mapping mode to guide precise lymphadenectomy. Numerous nanoprobes have been designed for multimodal LN mapping. Yang et al[29] designed perylene diimide probes of different sizes for LN positron emission tomography and photoacoustic imaging. Shi et al[30] designed a tumor-targeted CuS nanoparticle for LN fluorescence/computed tomography imaging and guided photothermal therapy. Le et al designed indocyanine green nanoimaging agent for metastatic lymph node detection with different size of polydopamine.[31] Despite advances in nanoprobe have been design, a critical gap persists: the absence of a single, stable nanoconstruct that seamlessly bridges preoperative planning with real-time intraoperative navigation. This fragmentation impedes surgical precision, demanding a unified platform enabling surgeons to "see before cutting and trace while cutting." Recent sophisticated polymer-based nanoprobes have indeed advanced multimodal imaging capabilities; for instance, some systems offer excellent performance in specific imaging modalities such as photoacoustic or fluorescence/computed tomography imaging[32] or demonstrate innovative drug delivery and imaging combinations.[33] However, a platform that integrates the full continuum from preoperative magnetic resonance planning to multiple, complementary intraoperative guidance modalities (optical, NIR fluorescence, thermal) within a single, size-tunable construct remains an unmet need. To address this unmet clinical need, we engineered a polydopamine nanoparticle (PDA NP) platform, leveraging its unique physicochemical properties for integrated LN mapping. With intriguing physicochemical properties, such as coloration,[34] easy functionalization,[35] high drug-loading efficacy,[36] high metal-chelation ability,[37] and ultrafast thermal relaxation,[38] PDA NPs have been widely applied in tumor biological imaging. Furthermore, by adjusting the pH in the dopamine self-assembly process, PDA NPs of different sizes can be easily obtained.[39]

In our previous research, we synthesized polydopamine (PDA)-based nanoparticles (NPs) incorporating polyethylene glycol (PEG), a tumor-targeting ligand comprising a cyclic arginine-glycine-aspartic acid sequence (cRGD), a near-infrared (NIR) organic dye (IR820), and the clinical MRI contrast agent $Gd(NH_2)_2$. This synthesis aimed to facilitate the development of precise and highly efficient photothermal therapy (PTT) for metastatic lymph nodes (LNs) in gastric

cancer in murine models. The findings from this study are pivotal for clinical translation. Building upon these results, we have initiated a preclinical study to evaluate the feasibility of precise lymphadenectomy by using PDA NPs (polyethylene glycol (PEG)-PDA@IR820/Gd(NH_2)$_2$, termed PPIG NPs), employing both preoperative and intraoperative LNs mapping modalities.[40] Furthermore, we engineered polypropylene glycol (PPIG) nanoparticles (NPs) of varying sizes to address diverse clinical scenarios. Recognizing that NPs within the 50–200 nm range preferentially drain into lymphatic vessels rather than the bloodstream,[41,42] we synthesized PPIG NPs in three distinct size categories: 50–100 nm, 100–150 nm, and 150–200 nm. These NPs are designed to specifically target LNs and lymphatic vessels, and exhibit differential residence times. This innovative and precise lymph node mapping approach has the potential to transform current clinical practices.

Materials and Methods

Chemistry

Dopamine hydrochloride (98%) (Aladdin, China), IR820 ($C_{46}H_{50}C_lN_2NaO_6S_2$, 80%, Aladdin, China), sodium hydrate (99%), and gadodiamide (OMNISCAN) were purchased from the Casmart and Rjmart platforms. PEG (NH_2-mPEG-NH_2, MW 5000, 98%) was obtained from Guangzhou Tanshui Co., Ltd. (Guangzhou, China). Dulbecco's minimum essential medium (DMEM), trypsin-containing ethylenediaminetetraacetic acid, fetal bovine serum, anti-CD3-PerCP-Cy5.5 (BD), anti-CD4-FITC (BD), and anti-CD8-PE (BD) antibodies, anti-CD11c-FITC (BD), anti-CD80-PE (BD), and anti-CD86-APC (BD) antibodies and penicillin-streptomycin solution were purchased from Thermo Fisher Scientific (MA). We obtained solutions of CCK-8, Hoechst 33342, and PBS from Beyotime (Shanghai, China). Deionized water (18.2 MΩ cm) was obtained using a water purification system (Synergy, Millipore, MA). TEM images were acquired using a JEOL JEM-2100F TEM. A Shimadzu UV-2600 UV-vis spectrophotometer was used to acquire UV-vis absorption spectra. Zeta potentials were measured using a Zetasizer Nano ZS (Malvern). We purchased 808 nm semiconductor lasers from Shanghai Xilong Optoelectronics Technology Co. Ltd. (China). *In-vivo* optical and NIR fluorescence imaging of the LNs in BALb/c mice was conducted using Digi-MIH-001 (DPM-I Beijing Precision Medicine Co., Ltd., Beijing, China) and DPM-ENDOCAM-01, DPM-LIHGT-01 (Zhuhai Dipu Medical Technology Co., Ltd)., respectively. Mouse LNs were imaged on a 3.0-T Philips Achieva clinical MRI scanner (Philips Healthcare, Best, The Netherlands). IR thermal images were acquired using an IR thermal camera (FLIR E50, USA).

Synthesis of Different-Sized Polydopamine Nanoparticles

Four hundred and thirty-two milligrams of dopamine hydrochloride (2.28 mmol) (Aladdin) was dissolved in 216 mL of deionized water. We obtained PDA NPs by adding 1 N NaOH solution to the dopamine hydrochloride solution under vigorous stirring at 50 °C. The solution gradually turned dark brown. After stirring for 10 h, the solution was centrifuged and washed with deionized water several times.

Size Control of Polydopamine Nanoparticles

We systematically varied the amount of NaOH from 456 to 2736 μL to examine the effects of the synthetic parameters.

Surface Modification of Polydopamine Nanoparticles with NH_2-PEG5000-NH_2 (PEG-PDA NPs)

We adjusted the pH of 10 mL of PDA aqueous solution (2 mg/mL of water) to 9. Then, 24 mg NH_2-PEG_{5000}-NH_2 was added to the solution. After vigorous stirring for 12 h, PEG-modified PDA was retrieved by centrifugation (12000 rpm for 10min, 26°C) and was washed with deionized water several times. Then, the aqueous solvent was removed by freeze-drying to obtain PEG-PDA powder.

Loading of the Polydopamine Nanoparticles with IR820 and Gadodiamide

We mixed freshly prepared IR820 solution with a PEG-PDA NP aqueous solution at an IR820/PEG-PDA NP weight ratio of 0.04:1 and left the mixture to react for 6 h in the dark. The formed NPs were centrifuged (12000 rpm for 10min, 26°C) and washed with deionized water several times. Unloaded, free IR820 was analyzed using a UV-vis-NIR spectrophotometer. The loading efficiency (weight of loaded IR820/weight of added IR820 × 100%) and loading content (weight of loaded IR820/(weight of loaded IR820 + weight of NPs) × 100%] of IR820 on the NPs were calculated. The photothermal properties of the different-sized NPs in 200 μL of PBS in Eppendorf tubes after irradiation with an 808 nm

NIR laser (FC-808-10W-MM, Xilong Company, Shanghai, China) at a power density of 0.125–1 W/cm^2 for 5 min were investigated. Real-time thermal images were recorded using an IR thermal camera (Fotric 225–1, Fotric). IR images were used to determine the corresponding temperature. The NPs thus generated were denoted as PEG-PDA@IR820/Gd$(NH_2)_2$ NPs (PPIG NPs).

In-vitro Studies

In-vitro Cellular Uptake Studies Using Electron Microscope

To determine the intracellular localization of PPI NPs, SVEC4-10 cells (1.0×10^4 cells/well) were incubated with PPI NPs at 37 °C for 24 h. Then, the cell nuclei were stained with Hoechst 33342. The cells were imaged using confocal laser scanning microscopy, using laser channels with excitation wavelengths of 455 and 773 nm to excite Hoechst 33342 and IR820, respectively.

In-vitro Cell Viability Assessment

The viability of cells treated with PPI NPs at different concentrations was measured using a CCK-8 colorimetric assay (Dojindo, Kumamoto, Japan). Briefly, SVEC4-10 cells (1.5×10^4 cells/well) were incubated with PPI NPs at different concentrations. Cells incubated with DMEM were included as a control. After a 24 h incubation, the medium was removed and the cells were washed with PBS and subjected to a the CCK-8 assay. The absorbance at 450 nm in each well was read using a microplate reader (SPARK 10 M, Tecan, NY, USA). For each sample, the mean and standard deviation of the measurements are reported.

In addition, the calcein AM/propidium iodide (PI) staining method was used to evaluate cell viability. SVEC4-10 cells were incubated with PEG-PDA NPs at different concentrations, and cells incubated with DMEM were included as a control. After 24 h, the cells were washed with PBS and stained with calcein AM/PI solution. Images were captured using an inverted microscope (IX73, Olympus, Tokyo, Japan).

In-vivo and Ex vivo Studies

In-vivo Multimodal Lymphatic System Imaging in Animal Models

Female BALb/c mice were obtained from the Biomedical Research Institute of Southern Medical University. Animal care and euthanasia were conducted with the approval of the Institutional Animal Care and Use Committee of Southern Medical University (certification No. K2020015) in accordance with the National Institutes of Health Guide for the Care and Use of Laboratory Animals. For LN optical imaging, the left rear footpad of mice (n = 3/group) was injected with 50 μL of PBS containing 0.75 mg of the different-sized PPI NPs. Mice were euthanized at designated time points, and their LNs were imaged using NIR fluorescence. For LN thermal imaging, mice were randomly divided into three groups (n = 3/group), injected with PPI NPs of different sizes, and irradiated with laser light (0.75 W/cm^2) for 10 min. Temperature changes in vivo were recorded in real time using an IR thermal camera (Fotric 225–1).

Optical and Near-Infrared Fluorescence Imaging in Human Specimens

This study was conducted in accordance with the principles of the Declaration of Helsinki and was approved by the Ethics Committee of Nanfang Hospital of Southern Medical University (Certification No. NFEC-2021-02-K1). All participating patients provided written informed consent prior to the study commencement. Human stomach and omentum specimens were obtained from anatomical specimens harvested during laparoscopic D2 distal gastrectomy surgery. PPIG NPs (15 mg/mL) were administered via four-point subserosal injections in the greater curvature of the human stomach. Optical and NIR fluorescence images of the LNs were collected using the Digi-MIH-001, DPM-ENDOCAM-01, and DPM-LIHGT-01 devices.

Ex vivo Analysis of Different Groups of Immune Cells

To examine the immune response caused by the PTT therapy, the lymph nodes were surgically resected from mice in different groups. Then lymphocytes in the lymph nodes were obtained after several operation. The collected lymphocytes were incubated with anti-CD3-PerCP-Cy5.5 (BD), anti-CD4-FITC (BD), and anti-CD8-PE (BD) antibodies according to the standard protocols, to determine the content of CD 4^+ or CD 8^+ T cells in the tumors and spleens using a flow

cytometry. The frequency of matured DCs in the lymph nodes was then examined by flow cytometry (BD FASCVerse, USA) after immunofluorescence staining with anti-CD11c-FITC (BD), anti-CD80-PE (BD), and anti-CD86-APC (BD) antibodies according to the procedure of the manufacturer.

In-vivo Biodistribution and Biosafety Analyses

For in vivo analysis of biodistribution, the left rear footpad of BALB/c mice (n = 3/group) was injected with 50 μL of PBS containing 0.75 mg of different-sized PPI NPs and an equal amount of IR820. At the time of the highest NIR fluorescence signal of the different-sized PPI NPs and IR820 dye after local injection, the mice were euthanized with an overdose of pentobarbital. The major organs (heart, liver, spleen, lungs, kidneys, brain, and LNs) were excised and imaged by Digi-MIH-001 (DPM-I Beijing Precision Medicine Co., Ltd., Beijing, China) and DPM-ENDOCAM-01, DPM-LIHGT-01 (Zhuhai Dipu Medical Technology Co., Ltd). To quantitatively and comparatively evaluate the toxicity of the different-sized PPI NPs, Balb/c (n = 3/group) were injected with 100 μL of PBS containing 1.5 mg of the different-sized PPI NPs. Biochemical blood indices, including alanine transaminase (ALT), aspartate transaminase (AST), blood urea nitrogen (BUN), and creatinine (CREA), were measured using corresponding ELISA kits (Sigma).

Statistical Analysis

Student's *t* test was used for comparisons between two groups. Oneway ANOVA with Fisher's LSD were used for multiple-group analysis. Time course analysis between groups was performed by general linear model repeated-measures analysis. $p < 0.05$ was considered to be statistical significance. The statistical tests were run with SPSS 24.0 (SPSS Inc., Chicago, IL).

Results

Design of Multi-Sized Polydopamine-Based Nanoparticles for Integrative Pre- and Intra-Operative Multimodal Lymph Node Mapping

The design of the PEG-PDA NPs of different sizes, consisting of PEG_{5000}-functionalized PDA NPs, the NIR dye IR820, and the clinical MRI contrast agent gadodiamide is shown in Figure 1. PDA NPs were selected as the optical image agent because of their black coloration, easy functionalization, high metal-ion chelation, and low systemic toxicity.[43] Different-sized PDA NPs were synthesized by varying the pH of the solution. PEG_{5000}, which is hydrophilic, was introduced in the outer shell of the PDA NPs to improve biocompatibility.[44] Finally, IR820 and gadodiamide were incorporated to allow the PEG-PDA to emit strong NIR fluorescence and T1-weighted image signals for sensitive LN imaging in vivo.[45,46] Following injection into the left hind footpad, the PPIG NPs drained specifically to the ipsilateral popliteal LN. Pre- and intra-operative multimodal LN mapping images were acquired, including MR/optical/NIR fluorescence/thermal images of the left popliteal LN. The PPIG NPs were also injected subserosally into the greater curvature of the human stomach. Optical and NIR fluorescence images of the LNs along the greater curvature were then acquired.

Preparation and Characterization of the Polydopamine-Based Nanoparticles

We first synthesized PDA NPs through the oxidation–polymerization of dopamine monomers in an alkaline environment. PDA NPs of different sizes were obtained by varying the amount of NaOH. As PDA is insoluble in phosphate-buffered saline (PBS), the application of PDA NPs in biological studies is limited. Therefore, we turned the PBS-soluble PDA NPs that had limited solubility into a PBS-soluble form via PEG modification. Stability experiments using non-PEG PDA and PEG-PDA NPs of different sizes at 0, 1, 6, 12, and 24 h are summarized in Supporting Information, Figure S1. PEG-PDA remained stable in PBS after 24 h, whereas non-PEG PDA was strongly precipitated. These results indicate that the PEG modification significantly improved PDA NP stability in PBS solution. After the washing and centrifuging steps, the NIR dye IR820 and clinical MRI contrast agent gadodiamide (OMNISCAN) were loaded onto the PEG-PDA NPs of different sizes. The resulting PPIG NPs were then characterized by transmission electron microscopy (TEM), dynamic light scattering (DLS), zeta potential measurement, ultraviolet-visible (UV-vis) spectral analysis, and T1 relaxation rate analysis. We successfully obtained a series of PPIG NPs with sizes of 87.2 ± 28.5 nm, 134.4 ± 45.4 nm, and 170.6 ± 53.7 nm, as confirmed by TEM and DLS (Figure 2a and b). The zeta potentials of the multi-sized PPIG NPs ranged from –

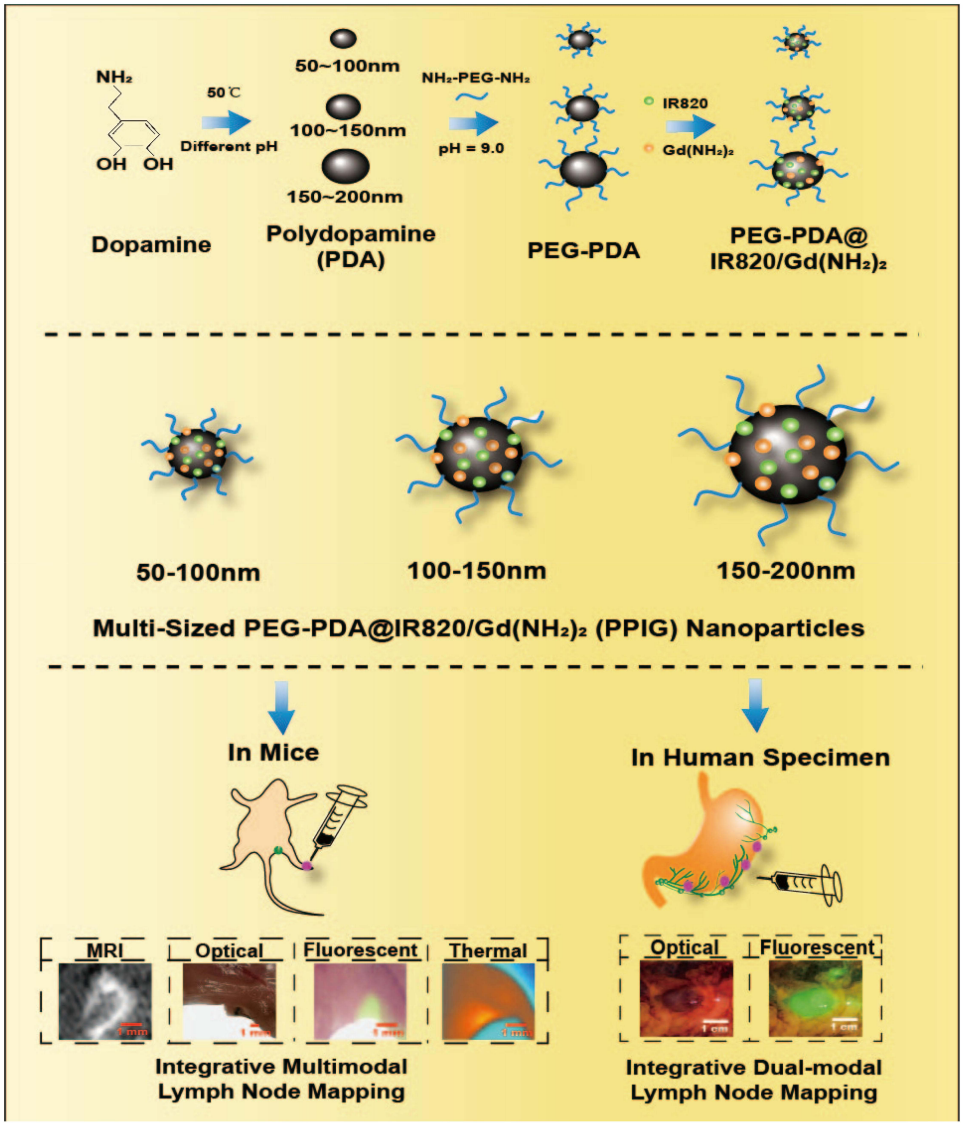

Figure 1 Design of PPIG NPs of different sizes for integrative multimodal LN mapping. Schematic illustration of the design and synthesis of multi-sized PEG-PDA@IR820/Gd $(NH_2)_2$ (PPIG) NPs. The PPIG NPs were injected into the left footpads of mice and were found to drain specifically to the left popliteal LN. MR/optical/NIR fluorescence/ thermal images of the left popliteal LN were acquired. PPIG NPs were injected subserosally into the greater curvature of the human stomach, and optical/NIR fluorescence images of the LNs along the greater curvature were then acquired.

38.7 to 43.6 eV (Figure 2c). The broadband UV-vis absorption of PDA is shown in Figure 2d. Due to the IR820 loading, a distinctive absorbance peak was observed at ~820 nm (Figure 2d). IR820 is absorbed onto the PPIGs by interacting with the particle surface. This interaction is driven by hydrogen bonding between the abundant catechol/amine groups on the PPIG backbone and the IR820 molecules. In addition, π–π stacking likely played a role in strengthening the interaction between the PPIGs and IR820. In the T1-weighted MRI performance evaluation, the MRI signal intensity of the PPIG NPs increased linearly with their concentration for all size groups (Figure 2e). The positive linear relationship between the quantitatively measured signals and NP concentrations is shown in Figure 2e. The Gd^{2+} content of the different-sized NPs, quantified by inductively coupled plasma mass spectrometry (ICP-MS), was 156.65 ± 12.1 ng/mL. PPIG exhibit high binding affinity toward various metal ions, attributed to the presence of abundant sites for metal coordination, including amine, carboxy, o-quinone, semiquinone, phenolic groups, and nitrogen atoms on their surface.[43]

The photothermal properties of the differently sized PPIG NPs were then evaluated. The temperatures of the laser-exposed solutions with the PPIG NPs of different sizes increased with nanoparticle size, nanoparticle concentration, and

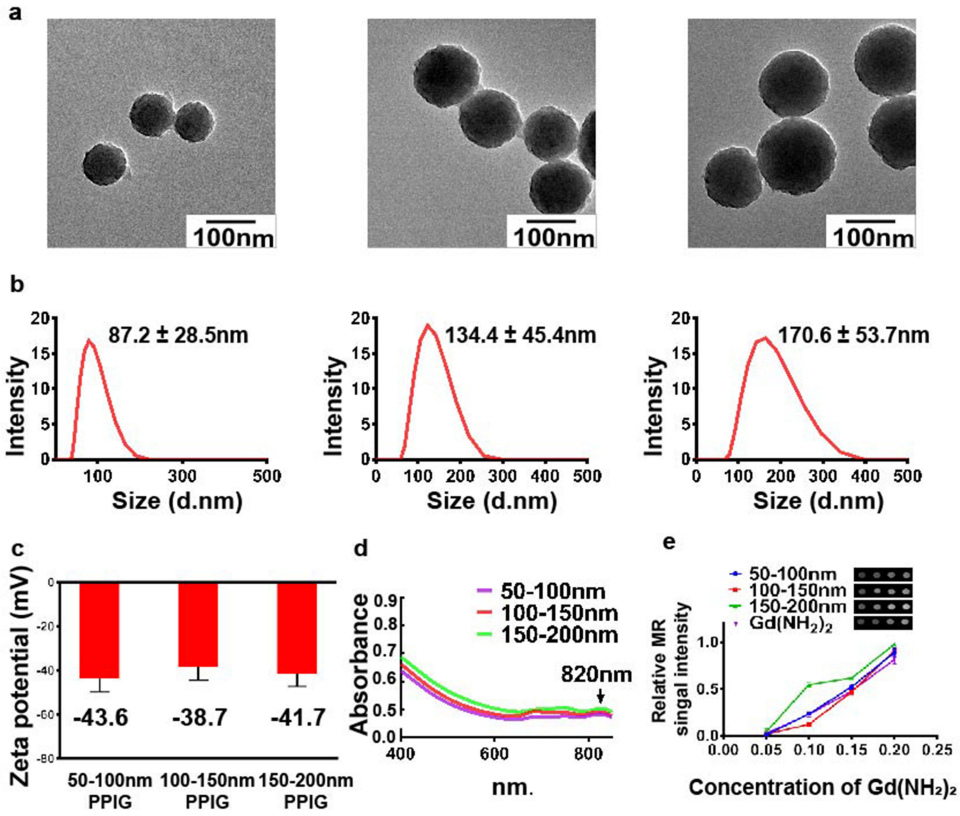

Figure 2 *In-vitro* characterization of the multi-sized PPIG NPs. (**a**) TEM image of the PPIG NPs of different sizes. Scale bar: 200 nm. (**b**) DLS results for the PPIG NPs of different sizes. (**c**) Zeta potentials of the PPIG NPs of different sizes. (**d**) UV-Vis-NIR spectra of the PPIG NPs of different sizes. (**e**) Relative MR signal intensities of the PPIG NPs of different sizes at various concentrations.

laser power density (Figures S2a–c). The temperature of the 150–200 nm PPIG NPs (400 μg/mL) solution rapidly increased to 40 °C at a power density of 1 W/cm^2. The thermal image became brighter with increasing NP concentration and laser power density. In the PBS buffer alone, no apparent increase in temperature was observed upon irradiation under the same conditions. The photothermal effect of the PPIG NPs was stable, with similar, high temperatures during five irradiation cycles (Figure S2d). These results indicated that PPIG NPs may serve as an effective photothermal agent.

In-vitro Cellular Uptake and Biosafety Assessment of Polydopamine-Based Nanoparticles

In-vitro cytocompatibility is essential for the application of nanomaterials in biomedical engineering. We selected SVEC4-10 cells (mouse axillary lymph-node/vascular epithelial cells, obtained from the American Type Culture Collection, ATCC) to evaluate the cellular uptake of the different-sized PPIG NPs using confocal laser scanning microscopy. PPIG NPs of all sizes were internalized and surrounded the cell nuclei (Supporting Information Figure S3a), implying cytoplasmic localization. The relative fluorescence of the SVEC4-10 cells was quantitatively analyzed (Supporting Information Figure S3b). These findings demonstrate that PPIG nanoparticles across different sizes can be efficiently absorbed by lymphatic/vascular endothelial cells.

To evaluate the cytotoxicity of PPIG NPs, we used calcein AM/propidium iodide (PI) staining, in which live and dead cells emit green and red fluorescence, respectively. After a 24-h incubation with PEG-PDA NPs, red-fluorescent cells were hardly observed (Supporting Information Figure S4a). Live-to-dead cell ratios are shown in Supporting Information Figure S4b. The results were in line with the calcein AM/PI staining results. Furthermore, we used a well-established CCK-8 method[47,48] to evaluate cytotoxicity after incubation with PPIG NPs (Supporting Information Figure S4c). The survival rates were more than 85% upon incubation with PPIG NPs of all sizes. These results indicated that PPIG NPs of all sizes are biologically safe.

https://doi.org/10.2147/IJN.S555760

In-vivo Multimodal Lymph Node Imaging Using Different-Sized Polydopamine-Based Nanoparticles

Size-dependent drainage of PPIG NPs into the lymphatic vessels was investigated in a mouse model after footpad injection. Proper volume samples (50 μL containing 0.75 mg of PPIG NPs of each size range per mouse) were injected into the left rear footpad of BALb/c mice (n = 3/group). The treated mice were allowed to move freely. At different time points after injection (1, 2, 4, 12, and 24 h), the mice were anesthetized and PPIG NP accumulation was investigated by MRI (Figure 3). In addition, the MR signal intensity in the left popliteal LN was determined, as shown in Supporting Information Figure S5. At 1 h post-injection, the popliteal LN was visualized for all groups of NPs. The 50–100 nm PPIG NPs group reached the highest MR signal intensity, and the signal intensity remarkably decreased within 4 h after injection. For the 100–150 nm PPIG NPs group, the highest signal intensity was observed at 4 h and lasted up to 12 h after injection. For the 150–200 nm PPIG NPs group, the highest MR signal intensity was observed at 12 h and lasted up to 24 h after injection. Tumors near the body surface, such as breast and skin cancers, can be imaged directly using MR-LAG. MR-LAG allows for the evaluation of the anatomical and functional status of lymphatic vessels and LNs.[49] However, traditional MR agents cannot differentiate lymphatic channels from superficial veins.[50] Therefore, MR-LAG for deep-seated tumors requires these agents to have rapid, LN-specific MR imaging capabilities. Moreover, traditional MR agents could not be detected during surgery, due to its transparent and colourless. Based on the above results, 50–100 nm PPIG NPs may be a more suitable MR-LAG agent for surface tumors such as head-and-neck tumors than traditional MR-LAG agents owing to their rapid MRI capability.[51] For deep-seated tumors, such as GC and colon-rectal cancers, MR-LAG must be performed under endoscopic procedure guidance. Accordingly, MR-LAR agents for deep-seated tumors require a relatively long lymphatic system retention time. This study showed that larger-sized PPIG NPs, such as those of 100–150 nm and 150–200 nm, have a relatively long lymphatic system retention time, ranging from 12–24 h. These results indicate that PPIG NPs of 100–200 nm may be suitable MR-LAR agents for deep-seated tumors.

For optical imaging, NPs of different sizes were injected into the left footpads of mice, and they were then sacrificed for imaging (Figure 4). In the 50–100 nm PPIG NPs group, the LNs were obviously stained at 1 h after injection, and the staining faded gradually over 4 h after injection. For the 100–150 nm and 150–200 nm PPIG NPs groups, the LNs were obviously stained at 2 h and 4 h after injection, respectively. Owing to their distinct optimal coloration kinetics, the different-sized PPIG-NPs may satisfy the different needs in various clinical scenarios. PPIG NPs have the same coloration ability as nano-carbon NPs. Unlike blue dyes, which may cause operative field interference, PPIG NPs and nano-carbon NPs can specifically enter lymph vessels.[52] Given their rapid diffusion time, 50–100 nm PPIGs could serve

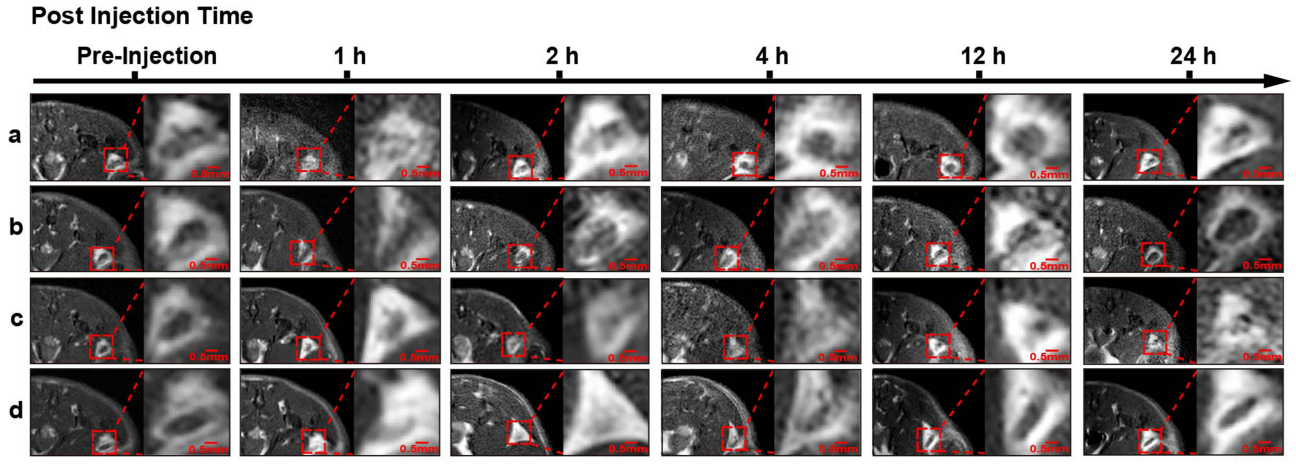

Figure 3 *In-vivo* mouse LN MR imaging using PPIG NPs of different sizes and $Gd(NH_2)_2$. *In-vivo* MR images of mouse LNs before and 1, 2, 4, 12, and 24 h after footpad injection of the PPIG NPs of different sizes. The red boxes indicate the LNs. (**a**) 50–100 nm PPIG group; (**b**) 100–150 nm PPIG group; (**c**) 150–200 nm PPIG group; (**d**) Gd $(NH_2)_2$ group.

https://doi.org/10.2147/IJN.S555760

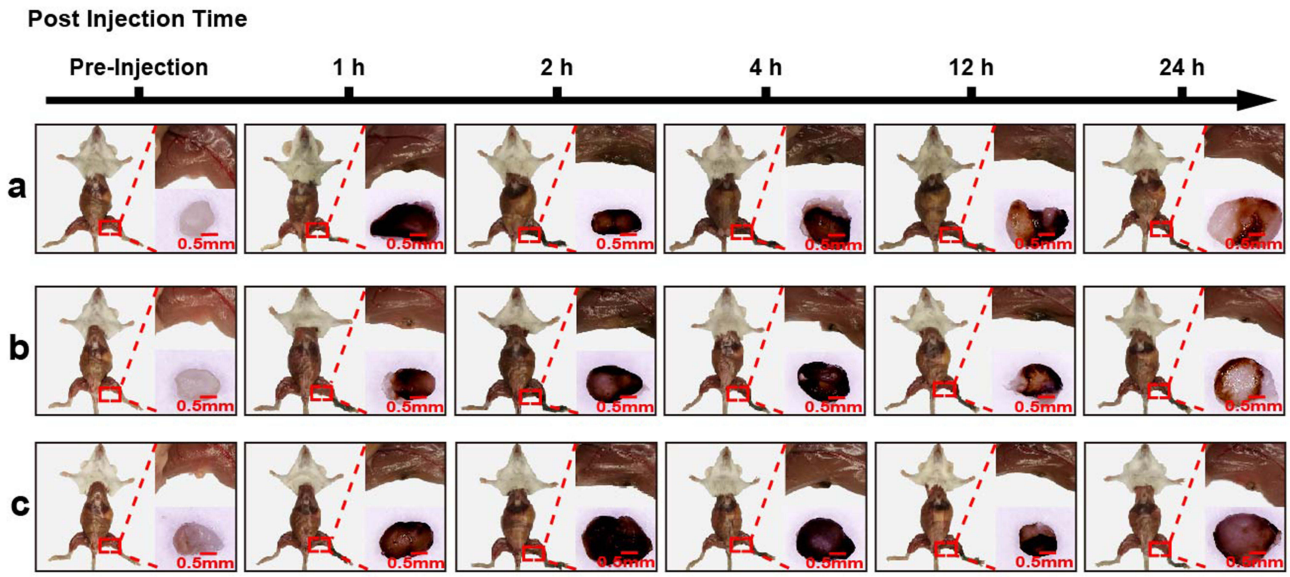

Figure 4 *In-vivo* mouse LN optical imaging using PPIG NPs of different sizes. *In-vivo* optical images of mouse LNs before and 1, 2, 4, 12, and 24 h after footpad injection of the different-sized PPIG NPs. The red boxes indicate the LNs. (**a**) 50–100 nm PPIG group; (**b**) 100–150 nm PPIG group; (**c**) 150–200 nm PPIG group.

as an intra-operative injection LN mapping dye, whereas 100–150 nm PPIG and 150–200 nm PPIG can be used for pre-operative injection given their relatively long residence times, which are similar to that of melanin.[53]

As multimodal imaging agents, the PPIG NPs were further employed for NIR fluorescence imaging. We investigated the accumulation tendency of the different-sized PPIG NPs in LNs. Different-sized PPIG NPs and an equal amount of free IR820 were injected into the left footpads of mice as mentioned previously and investigated using NIR fluorescence imaging before and at 1, 2, 4, 12, and 24 h after injection (Figure 5). The NIR fluorescence intensity in the left popliteal LN was determined (Figure S6). The trends in fluorescence intensity in the left popliteal LN were similar to those observed in the MRI. The 50–100 nm PPIG NPs group reached the highest NIR fluorescence intensity at 1 h after injection, and the signal intensity was remarkably decreased by 4 h after injection. For the 100–150 nm PPIG NPs group, the highest NIR fluorescence intensity was observed at 2 h and lasted until 12 h after injection. The 150–200 nm PPIG NPs group showed the highest NIR fluorescence intensity at 8 h, and the signal lasted for 24 h after injection. Free IR820 dye reached its peak NIR fluorescence intensity in the LN at 1 h, and the signal diffused into the periphery of the left popliteal LN and the blood system. NIR fluorescence techniques have been applied in medicine. Chi et al used NIR fluorescence to map the sentinel LN in breast cancer.[54] In 2020, the first human liver tumor surgery guided by NIR fluorescence was performed.[55] However, the small sizes of the NIR fluorescence dyes may not satisfy the needs for specific LN mapping during surgery. In this study, the NIR fluorescence imaging results indicated that pure NIR organic dyes such as IR820 may not be the best NIR fluorescence imaging agent for LN mapping because of the lack of lymphatic system specificity and the possibility of surgical field interference. Intra-operative dye injection is the mainstream for intra-operative LN mapping. Imaging agents require rapid, specific lymphatic system NIR fluorescence imaging capability. Thus, 50–100 nm PPIG NPs may be a suitable NIR agent for intra-operative injection. Due to the complexity of the draining lymphatic system, intact and adequate LN mapping is necessary, especially for GCs with multi-LN stations. However, intra-operative injection of LN mapping agents may extend the surgical time to achieve intact and adequate LN mapping. LN mapping using pre-operative injections of a NIR fluorescence imaging agent may be a promising approach, but it requires NIR fluorescence imaging agents to drain specifically into the lymphatic system and to have a relatively long lymphatic system retention time. In this study, the larger-sized PPIG NPs which were 100–150 nm and 150–200 nm, had relatively long lymphatic system retention times, ranging from 12–24 h. These results indicated that PPIG NPs of these sizes may be suitable NIR agents for LN mapping by pre-operative injection and may enable adequate GC LN mapping.

https://doi.org/10.2147/IJN.S555760

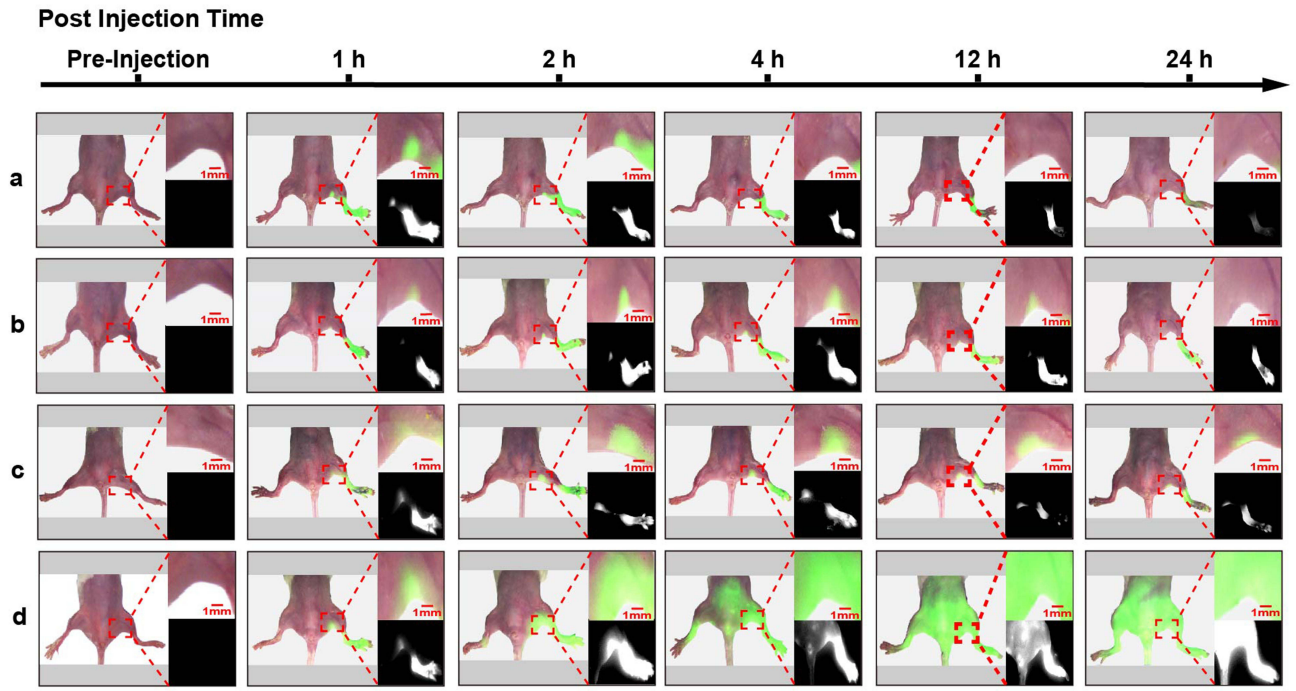

Figure 5 *In-vivo* mouse LN NIR fluorescence imaging using PPIG NPs of different sizes and IR820 dye. *In-vivo* NIR fluorescence images of mouse LNs before and 1, 2, 4, 12, and 24 h after footpad injection of the different-sized PPIG NPs and IR820 dye. (**a**) *In-vivo* mouse LN NIR fluorescence imaging using 50–100nm PPIG NPs; (**b**) *In-vivo* mouse LN NIR fluorescence imaging using 100–150nm PPIG NPs; (**c**) *In-vivo* mouse LN NIR fluorescence imaging using 150–200nm PPIG NPs; (**d**) *In-vivo* mouse LN NIR fluorescence imaging using IR820 dye. The red boxes indicate the LNs.

Finally, we studied the suitability of PPIG NPs for thermal image mapping. The different-sized PPIG NPs were injected into the left footpads of mice, as mentioned previously. The left popliteal LN of the mice was irradiated with 808 nm laser light (0.75 W/cm^2) at the time when the strongest NIR fluorescence signal was observed. During the process, an IR thermal camera was used to record the temperature on the LN surface. The left popliteal LN exhibited a pronounced increase in thermal signal under 808 nm laser irradiation, and this was maintained for 15 min (Figure 6). The temperature of the LNs treated with 50–100 nm PPIG NPs increased to 41.0 °C and was sustained for 10 min under irradiation (Supporting Information Figure S7). Thermal imaging using this approach may be suitable for mapping LNs in the abdomen. Photothermal therapy has emerged as a new paradigm by which to achieve precise cancer therapy for localized treatment owing to its ability to control irradiation and temperature in a non-invasive manner.[56] However, temperatures above 50 °C as used in photothermal therapy destroy both cancer cells and immunological cells.[57] LNs are critical secondary lymphoid organs in the immune system filled with immunological cells and thus, regular photothermal therapy with a temperature above 50 °C may not be suitable for LNs. A recent study revealed that low temperatures, around 45 °C, could be applied to produce a suitable tumor microenvironment for immunological responses and to enhance immunotherapeutic effects.[58,59]

In-vivo Biodistribution and Biosafety Evaluation of Different-Sized Polydopamine-Based Nanoparticles

BALb/c mice were injected in their footpads with PPIG NPs of different sizes to evaluate their biodistribution during LN mapping. At the time point with the highest NIR fluorescence signals for the PPIG NPs of all sizes and IR820, we sacrificed the mice with an overdose of pentobarbital. We then excised and imaged their major organs (heart, liver, spleen, lungs, kidneys, brain, and LNs) using DPM-ENDOCAM-01 and DPM-LIHGT-01 devices, as shown in Supporting Information Figure S8a. The NIR fluorescence images show that the different-sized PPIG NPs mostly accumulated in the left popliteal LN. Only a small amount of NIR fluorescence was observed in the metabolic organs,

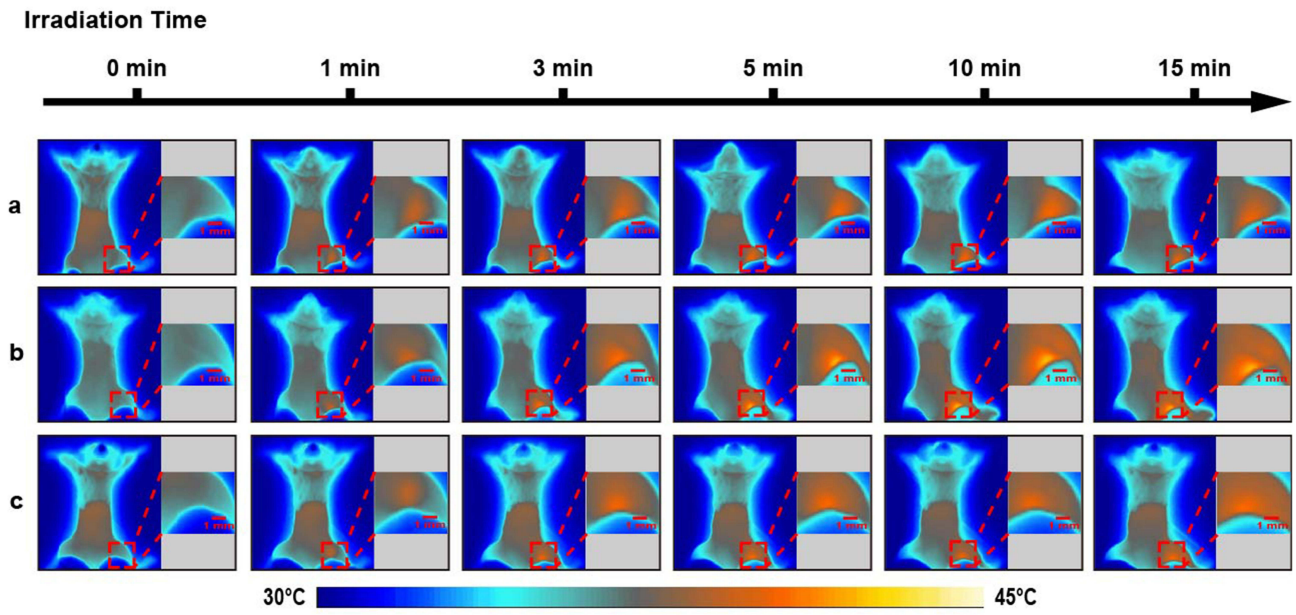

Figure 6 *In-vivo* mouse LN thermal imaging using PPIG NPs of different sizes. Thermal images of LNs in living mice treated with PPIG NPs of different sizes under 808 nm laser irradiation (0.75 W/cm^2) at 1, 2, and 8 h. (**a**) 50–100 nm PPIG group; (**b**) 100–150 nm PPIG group; (**c**) 150–200 nm PPIG group.

such as the liver and kidneys. These results validated the idea that PPIG NPs preferentially drained into the lymphatic vessels rather than entering the bloodstream after local injection.

Histological examination revealed that the major organs (liver, kidneys, spleen, heart, and brain) of the PPIG NP groups had no apparent histopathological damage (Figures S8a and S8b). Only the cortex of LNs was brown-yellow (Figure S8b). These results showed that the PPIG NPs of different sizes were mostly retained in the LNs, which was in line with the fluorescence results. To evaluate the biosafety of the PPIG NPs in vivo, we measured blood biochemistry indices, including ALT, AST, BUN, and CREA. ALT and AST are related to liver function, whereas the CREA and BUN levels are related to kidney function.[60] We found no significant differences in any of the indices of the treated Balb/c when compared to the untreated mice within an observation period of 1 month (Figure S9). These results suggested that the PPIG NPs have no obvious toxic effects on the liver and kidney functions.

In-vivo Lymphadenectomy Under Integrative Pre- and Intra-Operative Multimodal Lymph Node Mapping Guidance

Lymphadenectomies were performed under the guidance of integrative pre- and intra-operative LN mapping, using PPIG NPs. We injected 150–200 nm PPIG NPs in the left footpads of the mice and conducted pre-operative MRIs of the left popliteal LNs (Figure 7a). Then, lymphadenectomies of the left popliteal LN were performed under the guidance of optical/NIR fluorescence/thermal multimodal LN mapping (Figure 7b). Under the guidance of integrative pre- and intra-operative multimodal LN mapping, precise dissection of the left popliteal LN of the mice was achieved.

Preclinical Optical and Near-Infrared Fluorescence Lymph Node Imaging Using Polydopamine-Based Nanoparticles in Human Gastrointestinal Tumor Specimens

The utility of the PPIG NPs for optical/NIR fluorescence imaging for LN mapping was investigated in human gastrointestinal tumor specimens after subserosal injection for the first time. The PPIG NPs specifically drained through the lymphatic vessels rather than diffusing into normal tissues (Figure 8). After 30 min, the LNs along the greater curvature were black-stained and emitted green fluorescence under NIR irradiation, and the signals were even more pronounced at 60 min after injection. Thus, this study indicated that PPIG NPs could specifically enter the human

https://doi.org/10.2147/IJN.S555760

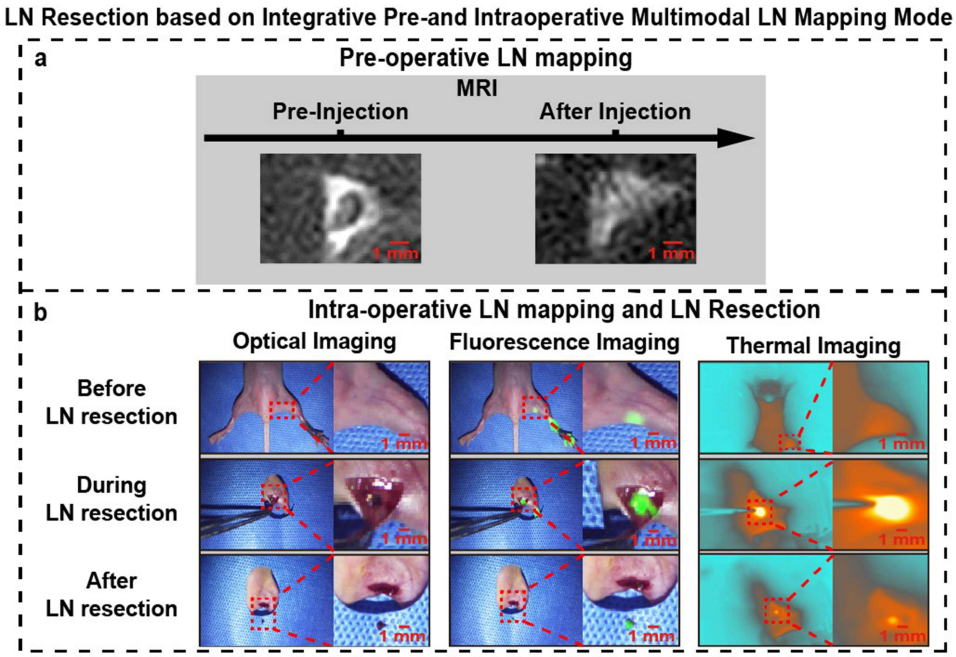

Figure 7 *In-vivo* mouse lymphadenectomy under integrative pre- and intra-operative MR/optical/NIR fluorescence/thermal multimodal LN imaging guidance. (**a**) PPIG NPs (150–200 nm) were injected into the left footpads of the mice, and integrative pre-operative LN MR images were acquired for up to 24 h. (**b**) Lymphadenectomy of the left popliteal LN was performed under the guidance of integrative intra-operative optical/NIR fluorescence/thermal multimodal LN imaging. Yellow arrows indicate LNs.

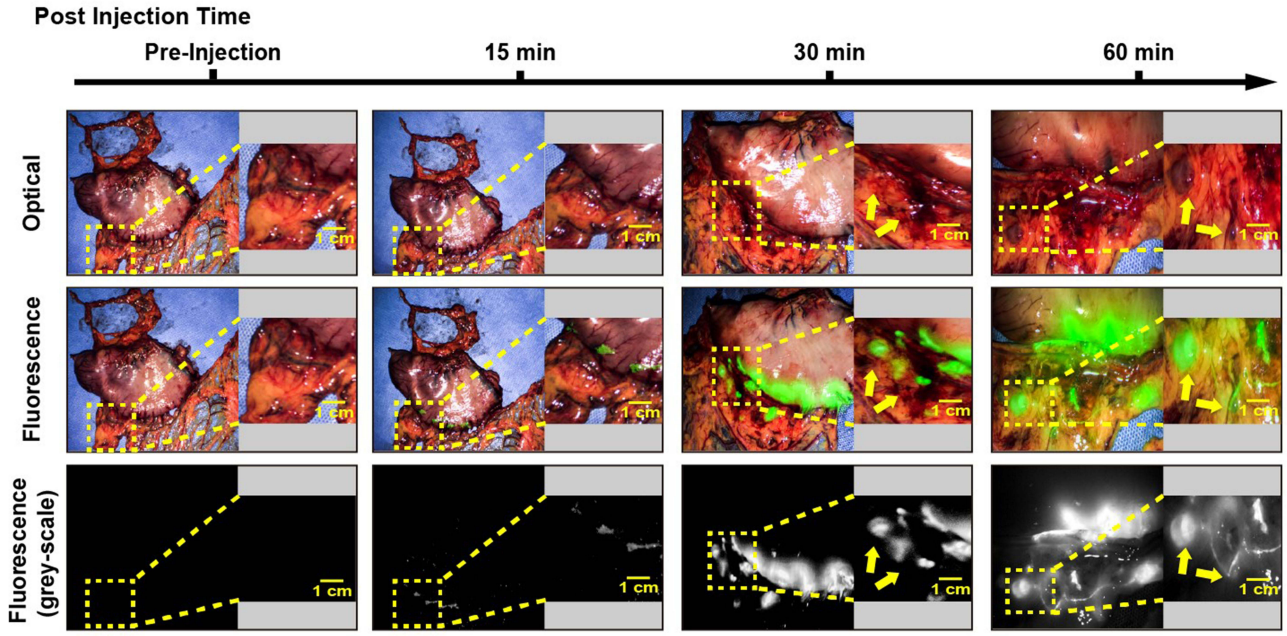

Figure 8 Optical/NIR fluorescence LN images of human gastrointestinal tumor specimens. Optical/NIR fluorescence LN images before and 15, 30, and 60 min after subserosal injection of the 50–100 nm PPIG NPs in the greater curvature of a human stomach. Yellow arrows indicate LNs.

lymphatic system. Moreover, we achieved optical/NIR fluorescence dual-modal LN imaging in human stomach specimens.

Next, we tested the utility of the PPIG NPs for optical/NIR fluorescence imaging for LN mapping in human colon specimens. Sixty minutes after the subserosal injection of 50–100 nm PPIG NPs, the LNs were mapped specifically (Supporting Information Figure S10).

Preclinical Simulation of Lymphadenectomy in Human Gastrointestinal Tumor Specimens

Building on the experimental findings in mice, we performed lymphadenectomies on human gastrointestinal tumor specimens. Our study encompassed 36 patients diagnosed with advanced gastric cancer, all of whom underwent laparoscopic radical distal gastrectomy. These patients were randomly and equally distributed into two groups PPIG NPs group and control group. In the PPIG NPs group, LNs were extracted using integrative optical/NIR fluorescence dual-modal LN mapping guidance from the isolated specimens. In the control group, LNs were extracted upon visual inspection by clinicians. Baseline characteristics of the patients are presented in Table 1. Our study demonstrates that LNs resection in the PPIG group significantly enhances the detection number of LNs compared to the control group (55.4 vs 36.8, $p < 0.05$).

Table 1 Basic Characteristics of PPIG NPs and Non-PPIG NPs Groups

Characteristic	No.(%)		*P* value
	PPIG NPs (N=18)	Non-PPIG NPs (N=18)	
Age,y Sex	62.3(11.7)	57.9(11.3)	0.26
Male	12(66.7)	10(55.6)	0.51
Female	6(33.3)	8(44.4)	
Tumor location			
Middle	2(11. 1)	4(22.2)	0.39
Lower	16(88.9)	14(77.8)	
Reconstruction method			
Billroth II	5 (27.8)	2(11. 1)	0.22
Roux-en-Y	13 (72.2)	16(88.9)	
Lauren classification			
Intestinal type	2(11. 1)	2(11. 1)	
Diffiuse type	11(61. 1)	12 (66.7)	0.78
Mixed type	5 (27.8)	4(22.2)	
Borrmann classification			
Fungating	1(5.6)	3(16.7)	
Ulcerated	16(88.9)	13 (72.2)	0.71
Diffiusely Infiltrative	1(5.6)	2(11. 1)	
Lymphovascular invasion			
Negative	8(44.4)	10(55.6)	0.52
Positive	10 (55.6)	8 (44.4)	
Size,cm			
≤3cm	6(33.3)	6(33.3)	1
>3cm	12 (66.7)	12 (66.7)	
pT stage			
pT3	10(55.6)	10(55.6)	1
pT4a	8(44.4)	8(44.4)	
pN stage			
pNO	2(11. 1)	5(27.8)	
pN1	4(22.2)	4(22.2)	
pN2	3(16.7)	4(22.2)	0.13
pN3a	4(22.2)	3(16.7)	
pN3b	5(27.8)	2(11. 1)	
Metastatic LNs	11.5(14.5)	5.2(8.3)	0.12
Total retrieved LNs	55.4(23.4)	36.8(12.7)	0.005
>30	17(94.4)	10(55.6)	0.006
≤30	1(5.6)	8(44.4)	

https://doi.org/10.2147/IJN.S555760

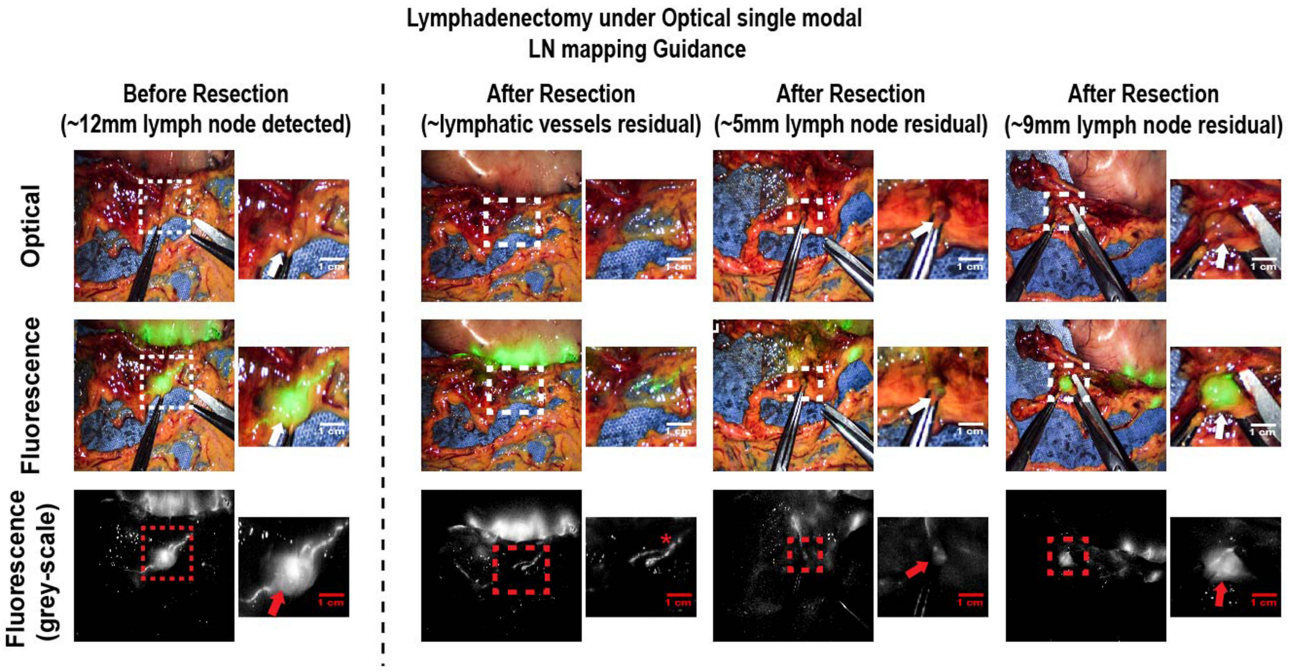

Figure 9 Preclinical simulation of a lymphadenectomy in a human gastrointestinal tumor specimen. PPIG NPs of 50–100 nm were subserosally injected in the greater curvature of the human stomach for 1 h. Then, lymphadenectomy of the LNs along the greater curvature was performed under the guidance of single-modal optical LN mapping guidance and integrative optical/NIR fluorescence dual-modal LN mapping guidance. White and Red arrows indicate LNs. Red asterisks indicate residual lymphatic tissue.

To further elucidate the technical advantages of optical/near-infrared (NIR) fluorescence dual-modal LN mapping. We initially administered peritumoral injections of PPIG NPs, followed by LN resection using optical mode. Subsequently, we employed NIR imaging to assess the residual lymphatic tissue (Figure 9). Our findings revealed the presence of residual lymphatic vessels post-lymphadenectomy, despite the resection of 12 mm LNs. Histopathological examinations confirmed the presence of residual lymphatic vessels (Figure S11). Additionally, we excised further residual lymph nodes (LNs) measuring approximately 5–9 mm within the remaining tissue. Consequently, this study suggests that lymphadenectomies guided by optical/near-infrared (NIR) fluorescence dual-modal lymph node mapping may enhance the detection of LNs and lymphatic tissue, thereby reducing the likelihood of missed LNs and lymphatic tissue. This approach is crucial for minimizing LN recurrence and improving the prognosis of patients with gastric cancer (GC).

Discussion

Accurate lymph node (LN) mapping is pivotal for precise lymphadenectomy in gastric cancer surgery. Current clinical practice, however, relies on fragmentary imaging modalities that operate in isolation during pre- and intra-operative phases. This disconnect often leads to inconsistencies in LN identification and staging, potentially compromising surgical outcomes. For instance, while magnetic resonance imaging (MRI) provides detailed anatomical information preoperatively, its contrast agents are not visible during surgery. Conversely, intraoperative agents like carbon nanoparticles and indocyanine green (ICG) offer real-time visualization but lack preoperative planning capability and suffer from limitations such as poor tissue penetration and nonspecific diffusion, respectively.

In this study, we developed a unified platform using polydopamine-based nanoparticles (PPIG NPs) that seamlessly bridges preoperative planning with intraoperative navigation. Unlike conventional single-modal agents, PPIG NPs enable integrative multimodal imaging encompassing MRI, optical, near-infrared (NIR) fluorescence, and thermal modalities. This integrated approach addresses the critical clinical need for consistent LN mapping across surgical phases, allowing surgeons to "see before cutting and trace while cutting." Our findings demonstrate that PPIG NPs not only enhance LN detection rates but also facilitate the precise delineation of lymphatic vessels, which are often the primary routes for metastatic spread in gastric cancer.

The PPIG NP platform presents distinct advantages over existing LN mapping techniques (Figure 7). First, it uniquely enables both preoperative MRI planning and real-time intraoperative visualization within a single agent. Second, it combines the strong optical coloration necessary for surgical visualization with complementary multimodal imaging capabilities. Third, its nanoparticle design ensures controlled lymphatic retention, minimizing the nonspecific diffusion that plagues small-molecule dyes like ICG. Finally, the incorporated photothermal properties allow for specific LN targeting and thermal contrast enhancement.

Beyond improved LN detection, our study demonstrates the potential of PPIG NPs for lymphatic vessel mapping (Figure 9 and S10, S11). In gastric cancer, lymphatic vessel infiltration frequently precedes LN metastasis and significantly influences patient prognosis.[61] The ability to precisely visualize these vessels intraoperatively could guide more targeted dissections and potentially identify micrometastases that might otherwise be missed. A previous randomized controlled trial demonstrated that prophylactic extended lymph node dissection did not improve survival in patients with advanced gastric cancer (AGC) and was associated with longer operative times and greater blood loss.[62] Nevertheless, pathologically confirmed distant lymph node metastases—such as those in para-aortic nodes—are still found in approximately 8.5% of AGC patients despite negative preoperative imaging. Retrieving deep-seated lymph nodes remains a surgical challenge. In this context, dissecting the associated lymphatic vessels followed by intraoperative frozen-section analysis could represent a minimally invasive and feasible strategy to determine whether extended lymphadenectomy is warranted. Successfully implementing this approach, however, depends on accurate real-time mapping of lymphatic vessels during surgery. The size-tunable design of our PPIG nanoparticles enhances their potential to meet this clinical need: smaller NPs (50–100 nm) rapidly diffuse within the lymphatic system, making them suitable for intraoperative guidance, whereas larger NPs (150–200 nm) exhibit prolonged retention and may be advantageous for preoperative planning and sustained intraoperative tracing. This capability addresses a critical gap in current surgical oncology, where lymphatic vessel mapping remains largely unexplored despite its clinical significance.

Notably, the application of PPIG NPs in human specimens yielded promising results. The significantly higher LN yield in the PPIG group compared to conventional visual inspection (55.4 vs 36.8, $p < 0.05$) underscores the practical utility of this approach. Furthermore, the identification of residual lymphatic tissue post-dissection highlights the potential for reducing missed metastases and improving surgical completeness.

While our findings are promising, several limitations warrant consideration. First, due to biosafety constraints, we were unable to evaluate MR and thermal LN mapping in human specimens. Future clinical trials will be essential to validate these modalities in human subjects. Second, although PPIG NPs with 24-hour retention represent an improvement over existing agents, this duration may still be insufficient for certain clinical workflows requiring longer intervals between administration and surgery. Development of nanoparticles with extended retention times while maintaining multimodal functionality would address this limitation. Third, the clinical significance of precise intraoperative lymphatic vessel identification requires further investigation. Future studies should explore correlations between mapped lymphatic vessels and patterns of metastatic spread, potentially identifying specific vessel pathways that correlate with poor prognosis. Additionally, research into whether lymphatic vessel mapping can guide the extent of lymphadenectomy or identify patients who would benefit from extended dissections would be valuable. Finally, the long-term biosafety and clearance pathways of PPIG NPs require comprehensive evaluation. While our short-term studies demonstrated good biocompatibility, systematic toxicological assessments and investigations into biodegradation mechanisms will be crucial for clinical translation.

Future research should focus on: (1) optimizing nanoparticle formulations for extended lymphatic retention; (2) developing targeted versions that specifically bind to metastatic LN markers; (3) integrating artificial intelligence algorithms to enhance image interpretation; and (4) conducting multicenter clinical trials to validate efficacy across diverse patient populations.

Conclusion

This study establishes a polydopamine-based nanoparticle platform that provides seamless, multimodal lymph-node mapping across the pre- and intra-operative phases, addressing the critical gap between surgical planning and real-time navigation. The system uniquely combines MRI, optical, NIR-fluorescence, and thermal imaging, while its size-tunable

design offers flexible lymphatic kinetics tailored to different clinical scenarios. It significantly enhanced lymph-node yield in human specimens and enabled unprecedented visualization of lymphatic vessels—a key route for metastasis. Future efforts should aim to extend nanoparticle retention, validate the approach in clinical trials, and explore targeted theranostic applications. With further development and clinical validation, this integrated platform has the potential to enhance the precision and completeness of lymphadenectomy, which may translate into improved oncologic outcomes for patients undergoing gastric cancer surgery.

Abbreviations

LN, lymph-node; GC, gastric cancer; MRI, magnetic resonance imaging; MR-LAG, magnetic resonance lymphangiography; NIR, near-infrared; ICG, indocyanine green; PDA, Polydopamine; PPIG, polyethylene glycol (PEG)-PDA@IR820/Gd$(NH_2)_2$.

Data Sharing Statement

The raw/processed data required to reproduce these findings cannot be shared at this time as the data also forms part of an ongoing study.

Acknowledgment

The authors want to thank Dr. Bingxia Zhao from the Southern Medical University for technical support. The authors would like to acknowledge the instrumental and technical support of Multimodal Biomedical Imaging Experimental Platform, Institute of Automation, Chinese Academy of Sciences.

Author Contributions

All authors made a significant contribution to the work reported, whether that is in the conception, study design, execution, acquisition of data, analysis and interpretation, or in all these areas; took part in drafting, revising or critically reviewing the article; gave final approval of the version to be published; have agreed on the journal to which the article has been submitted; and agree to be accountable for all aspects of the work.

Funding

This work was supported by grants from the National Natural Science Foundation of China (82001948; 81971746; 82103150; 82373240), the Guangdong Provincial Key Laboratory of Precision Medicine for Gastrointestinal Cancer (2020B121201004), Medical Scientific Research Foundation of Guangdong Province of China (A2020297), Key Clinical Technique of Guangzhou (2023P-ZD01), Outstanding Youths Development Scheme of Nanfang Hospital, Southern Medical University (2022J004), College Students' Innovative Entrepreneurial Training Plan Program (S202012121020; S202012121051; S202212121105; S202212121099).

Disclosure

The authors declare that they have no competing interests.

References

1. Sung H, Ferlay J, Siegel RL, et al. Global cancer statistics 2020: GLOBOCAN estimates of incidence and mortality worldwide for 36 cancers in 185 countries. *CA: a Cancer Journal for Clinicians*. 2021;71(3):209–249. doi:10.3322/caac.21660
2. Huang C, Liu H, Hu Y, et al. Laparoscopic vs open distal gastrectomy for locally advanced gastric cancer: five-year outcomes from the CLASS-01 randomized clinical trial. *JAMA Surg*. 2022;157(1):9–17. doi:10.1001/jamasurg.2021.5104
3. Chen QY, Zhong Q, Liu ZY, et al. Indocyanine green fluorescence imaging-guided versus conventional laparoscopic lymphadenectomy for gastric cancer: long-term outcomes of a phase 3 randomised clinical trial. *Nat Commun*. 2023;14(1):7413. doi:10.1038/s41467-023-42712-6
4. Ajani JA, D'Amico TA, Almhanna K, et al. Gastric cancer, version 3.2020, NCCN clinical practice guidelines in oncology. *J Nation Comprehen Canc Net*. 2016;14(10):1286–312.
5. Colen RR, Vangel M, Wang J, et al. Imaging genomic mapping of an invasive MRI phenotype predicts patient outcome and metabolic dysfunction: a TCGA glioma phenotype research group project. *BMC Medical Genomics*. 2014;7:30.

6. Sutton E, Braunstein L, El-Tamer M, et al. Accuracy of magnetic resonance imaging-guided biopsy to verify breast cancer pathologic complete response after neoadjuvant chemotherapy: a nonrandomized controlled trial. *JAMA Network Open*. 2021;4(1):e2034045. doi:10.1001/jamanetworkopen.2020.34045
7. Sohn KM, Lee JM, Lee SY, Ahn BY, Park SM, Kim KM. Comparing MR imaging and CT in the staging of gastric carcinoma. *AJR Am J Roentgenol*. 2000;174(6):1551–1557. doi:10.2214/ajr.174.6.1741551
8. Kim AY, Han JK, Seong CK, Kim TK, Choi BI. MRI in staging advanced gastric cancer: is it useful compared with spiral CT? *J Comp Assist Tomograph*. 2000;24(3):389–394. doi:10.1097/00004728-200005000-00006
9. Hasbahceci M, Akcakaya A, Memmi N, et al. Diffusion MRI on lymph node staging of gastric adenocarcinoma. *Quant Imag Med Surg*. 2015;5(3):392–400. doi:10.3978/j.issn.2223-4292.2015.03.06
10. Giganti F, Orsenigo E, Arcidiacono PG, et al. Preoperative locoregional staging of gastric cancer: is there a place for magnetic resonance imaging? Prospective comparison with EUS and multidetector computed tomography. *Gastric Cancer*. 2016;19(1):216–225. doi:10.1007/s10120-015-0468-1
11. Di Paola V, Mazzotta G, Conti M, et al. Image-Guided localization techniques for metastatic axillary lymph nodes in breast cancer; what radiologists should know. *Cancers (Basel)*. 2023;15(7):2130. doi:10.3390/cancers15072130
12. Li J, Deng X, Wang L, Liu J, Xu K. Clinical application of carbon nanoparticles in lymphatic mapping during colorectal cancer surgeries: a systematic review and meta-analysis. *Digest Liver Dis*. 2020;52(12):1445–1454. doi:10.1016/j.dld.2020.08.020
13. Woods R, Camp M, Durr N, Harvey S. A review of options for localization of axillary lymph nodes in the treatment of invasive breast cancer. *Academic Radiology*. 2019;26(6):805–819. doi:10.1016/j.acra.2018.07.002
14. Manolova V, Flace A, Bauer M, Schwarz K, Saudan P, Bachmann MF. Nanoparticles target distinct dendritic cell populations according to their size. *Eur J mmunol*. 2008;38(5):1404–1413. doi:10.1002/eji.200737984
15. Ke X, Howard G, Tang H, et al. Physical and chemical profiles of nanoparticles for lymphatic targeting. *Advanc Drug Deliver Rev*. 2019;151-152:72–93. doi:10.1016/j.addr.2019.09.005
16. Zhang Y, Lin S, Wang X, Zhu G. Nanovaccines for cancer immunotherapy. *Wiley Interdiscip Rev Nanomed Nanobiotechnol*. 2019;11(5):e1559. doi:10.1002/wnan.1559
17. Yashiro M, Matsuoka T. Sentinel node navigation surgery for gastric cancer: overview and perspective. *World J Gastrointest Surg*. 2015;7(1):1–9. doi:10.4240/wjgs.v7.i1.1
18. Dong J, Ma Q. Integration of inflammation, fibrosis, and cancer induced by carbon nanotubes. *Nanotoxicology*. 2019;13(9):1244–1274. doi:10.1080/17435390.2019.1651920
19. Escobedo J, Rusin O, Lim S, Strongin R. NIR dyes for bioimaging applications. *Curr Opin Chem Biol*. 2010;14(1):64–70. doi:10.1016/j.cbpa.2009.10.022
20. Miyashiro I. What is the problem in clinical application of sentinel node concept to gastric cancer surgery? *J Gastric Canc*. 2012;12(1):7–12. doi:10.5230/jgc.2012.12.1.7
21. Miyashiro I, Hiratsuka M, Sasako M, et al. High false-negative proportion of intraoperative histological examination as a serious problem for clinical application of sentinel node biopsy for early gastric cancer: final results of the Japan Clinical Oncology Group multicenter trial JCOG0302. *Gastric Cancer*. 2014;17(2):316–323. doi:10.1007/s10120-013-0285-3
22. Kwon I, Son T, Kim H, Hyung W. Fluorescent lymphography-guided lymphadenectomy during robotic radical gastrectomy for gastric cancer. *JAMA Surgery*. 2019;154(2):150–158. doi:10.1001/jamasurg.2018.4267
23. Chen Q, Xie J, Zhong Q, et al. Safety and efficacy of indocyanine green tracer-guided lymph node dissection during laparoscopic radical gastrectomy in patients with gastric cancer: a randomized clinical trial. *JAMA Surgery*. 2020;155(4):300–311. doi:10.1001/jamasurg.2019.6033
24. DMR-IR. Available from: http://visual.ic.uff.br/dmi. Accessed April 16, 2019.
25. Hakim A, Awale RN. Thermal imaging - an emerging modality for breast cancer detection: a comprehensive review. *J Med Sys*. 2020;44(8):136. doi:10.1007/s10916-020-01581-y
26. Magalhaes C, Vardasca R, Mendes J. Recent use of medical infrared thermography in skin neoplasms. *Skin Res Technol*. 2018;24(4):587–591. doi:10.1111/srt.12469
27. Michel U, Hornstein OP, Schönberger A. Thermographico-histologic study of the lymph drainage areas in malignant melanoma. *Der Hautarzt*. 1986;37(1):12–16.
28. Tao CS, Dong F, Wang DC, Guo CB. Diagnostic test for detection of cervical lymph node metastasis from oral squamous cell carcinoma via infrared thermal imaging. *Beijing da xue Xue Bao Yi Xue Ban*. 2019;51(5):959–963. doi:10.19723/j.issn.1671-167X.2019.05.028
29. Yang Z, Tian R, Wu J, et al. Impact of semiconducting perylene diimide nanoparticle size on lymph node mapping and cancer imaging. *ACS Nano*. 2017;11(4):4247–4255. doi:10.1021/acsnano.7b01261
30. Shi H, Yan R, Wu L, et al. Tumor-targeting CuS nanoparticles for multimodal imaging and guided photothermal therapy of lymph node metastasis. *Acta Biomaterialia*. 2018;72:256–265. doi:10.1016/j.actbio.2018.03.035
31. Le QV, Kang S, Lee J, et al. Size-Dependent effect of indocyanine green nanoimaging agent for metastatic lymph node detection. *Biomater Res*. 2024;28:0022. doi:10.34133/bmr.0022
32. Li X, Duan Z, Chen X, et al. Impairing tumor metabolic plasticity via a stable metal-phenolic-based polymeric nanomedicine to suppress colorectal cancer. *Adv Mater*. 2023;35(23):e2300548. doi:10.1002/adma.202300548
33. Wang X, Chen J, Li Z, et al. A branched polymer-based agent for efficient and precise targeting of fibrosis diseases by magnetic resonance imaging. *J Control Release*. 2024;373:905–916. doi:10.1016/j.jconrel.2024.07.072
34. Simon JD, Peles DN. The red and the black. *Account Chem Res*. 2010;43(11):1452–1460. doi:10.1021/ar100079y
35. Lee H, Dellatore SM, Miller WM, Messersmith PB. Mussel-inspired surface chemistry for multifunctional coatings. *Science*. 2007;318(5849):426–430.
36. Poinard B, Neo SZY, Yeo ELL, Heng HPS, Neoh KG, Kah JCY. Polydopamine nanoparticles enhance drug release for combined photodynamic and photothermal therapy. *ACS Appl Mat Interface*. 2018;10(25):21125–21136. doi:10.1021/acsami.8b04799
37. Hong L, Simon JD. Current understanding of the binding sites, capacity, affinity, and biological significance of metals in melanin. *J Phys Chem B*. 2007;111(28):7938–7947. doi:10.1021/jp071439h
38. Meng S, Kaxiras E. Mechanisms for ultrafast nonradiative relaxation in electronically excited eumelanin constituents. *Biophysical J*. 2008;95(9):4396–4402. doi:10.1529/biophysj.108.135756

39. Ju KY, Lee Y, Lee S, Park SB, Lee JK. Bioinspired polymerization of dopamine to generate melanin-like nanoparticles having an excellent free-radical-scavenging property. *Biomacromolecules*. 2011;12(3):625–632. doi:10.1021/bm101281b
40. Liang Y, Guo W, Li C, et al. Tumor-Targeted polydopamine-based nanoparticles for multimodal mapping following photothermal therapy of metastatic lymph nodes. *Int J Nanomedicine*. 2022;17:4659–4675. doi:10.2147/IJN.S367975
41. Fu C, Zhou H, Wang Y, et al. One-pot synthesis of dextran-coated iron oxide nanoclusters for real-time regional lymph node mapping. *Int J Nanomed*. 2017;12:3365–3374. doi:10.2147/IJN.S130322
42. Jiang H, Wang Q, Sun X. Lymph node targeting strategies to improve vaccination efficacy. *J Controlled Release*. 2017;267:47–56. doi:10.1016/j.jconrel.2017.08.009
43. Liu H, Yang Y, Liu Y, et al. Melanin-Like nanomaterials for advanced biomedical applications: a versatile platform with extraordinary promise. *Advanced Science*. 2020;7(7):1903129. doi:10.1002/advs.201903129
44. Liopo A, Su R, Oraevsky AA. Melanin nanoparticles as a novel contrast agent for optoacoustic tomography. *Photoacoustics*. 2015;3(1):35–43. doi:10.1016/j.pacs.2015.02.001
45. Fernandez-Fernandez A, Manchanda R, Lei T, et al. Comparative study of the optical and heat generation properties of IR820 and indocyanine green. *Mol Imaging*. 2012;11(2):99–113. doi:10.2310/7290.2011.00031
46. Lohrmann C, Földi E, Bartholomä JP, Langer M. MR imaging of the lymphatic system: distribution and contrast enhancement of gadodiamide after intradermal injection. *Lymphology*. 2006;39(4):156–163.
47. Hong Z, Feng H, Bu L. Melanin-based nanomaterials: the promising nanoplatforms for cancer diagnosis and therapy. *Nanomedicine*. 2020;28:102211. doi:10.1016/j.nano.2020.102211
48. Ge C, Du J, Zhao L, et al. Binding of blood proteins to carbon nanotubes reduces cytotoxicity. *Proceed Nation Acad Sci United States America*. 2011;108(41):16968–16973.
49. Liu N, Zhang Y. Magnetic resonance lymphangiography for the study of lymphatic system in lymphedema. *J Reconstruct Microsurg*. 2016;32(1):66–71.
50. Mitsumori LM, McDonald ES, Neligan PC, Maki JH. Peripheral magnetic resonance lymphangiography: techniques and applications. *Techniq Vascul Intervention Radiol*. 2016;19(4):262–272. doi:10.1053/j.tvir.2016.10.007
51. Loo BW Jr, Draney MT, Sivanandan R, et al. Indirect MR lymphangiography of the head and neck using conventional gadolinium contrast: a pilot study in humans. *Int J Radiat Oncol Biol Phys*. 2006;66(2):462–468. doi:10.1016/j.ijrobp.2006.05.045
52. Zhang L, Huang Y, Yang C, et al. Application of a carbon nanoparticle suspension for sentinel lymph node mapping in patients with early breast cancer: a retrospective cohort study. *World J Surg Oncol*. 2018;16(1):112. doi:10.1186/s12957-018-1414-6
53. Chu M, Hai W, Zhang Z, et al. Melanin nanoparticles derived from a homology of medicine and food for sentinel lymph node mapping and photothermal in vivo cancer therapy. *Biomaterials*. 2016;91:182–199. doi:10.1016/j.biomaterials.2016.03.018
54. Chi C, Ye J, Ding H, et al. Use of indocyanine green for detecting the sentinel lymph node in breast cancer patients: from preclinical evaluation to clinical validation. *PLoS One*. 2013;8(12):e83927. doi:10.1371/journal.pone.0083927
55. Hu Z, Fang C, Li B, et al. First-in-human liver-tumour surgery guided by multispectral fluorescence imaging in the visible and near-infrared-I/II windows. *Nat Biomed Engineer*. 2020;4(3):259–271. doi:10.1038/s41551-019-0494-0
56. Yu S, Wang C, Yu J, et al. Injectable bioresponsive gel depot for enhanced immune checkpoint blockade. *Advanc Mat*. 2018;30(28):e1801527. doi:10.1002/adma.201801527
57. Wang C, Xu L, Liang C, Xiang J, Peng R, Liu Z. Immunological responses triggered by photothermal therapy with carbon nanotubes in combination with anti-CTLA-4 therapy to inhibit cancer metastasis. *Advanced Materials*. 2014;26(48):8154–8162. doi:10.1002/adma.201402996
58. Li Y, He L, Dong H, et al. Fever-Inspired immunotherapy based on photothermal CpG nanotherapeutics: the critical role of mild heat in regulating tumor microenvironment. *Advanced Science*. 2018;5(6):1700805. doi:10.1002/advs.201700805
59. Huang L, Li Y, Du Y, et al. Mild photothermal therapy potentiates anti-PD-L1 treatment for immunologically cold tumors via an all-in-one and all-in-control strategy. *Nat Commun*. 2019;10(1):4871. doi:10.1038/s41467-019-12771-9
60. Jayapaul J, Arns S, Bunker M, et al. In vivo evaluation of riboflavin receptor targeted fluorescent USPIO in mice with prostate cancer xenografts. *Nano Research*. 2016;9(5):1319–1333. doi:10.1007/s12274-016-1028-7
61. Wang Y, Li X, Zhang T, et al. Neutrophils promote tumor invasion via FAM3C-mediated epithelial-to-mesenchymal transition in gastric cancer. *Int J Biol Sci*. 2023;19(5):1352–1368. doi:10.7150/ijbs.79022
62. Sasako M, Sano T, Yamamoto S, et al. D2 lymphadenectomy alone or with para-aortic nodal dissection for gastric cancer. *N Engl J Med*. 2008;359(5):453–462. doi:10.1056/NEJMoa0707035